Chinese Physics Letters **40**, 057101 (2023) **Express Letter**

Electron-Exciton Coupling in 1T-$TiSe_2$ Bilayer

Li Zhu(朱立)[1†], Wei-Min Zhao(赵伟民)[1†], Zhen-Yu Jia(贾振宇)[1], Huiping Li(李慧平)[2,3], Xuedong Xie(谢学栋)[1], Qi-Yuan Li(李启远)[1], Qi-Wei Wang(汪琪玮)[1], Li-Guo Dou(窦立国)[1], Ju-Gang Hu(胡聚罡)[1], Yi Zhang(张翼)[1], Wenguang Zhu(朱文光)[2,3], Shun-Li Yu(于顺利)[1*], Jian-Xin Li(李建新)[1*], and Shao-Chun Li(李绍春)[1,4*]

[1]*National Laboratory of Solid State Microstructures, Collaborative Innovation Center of Advanced Microstructures, School of Physics, Nanjing University, Nanjing 210093, China*
[2]*International Center for Quantum Design of Functional Materials (ICQD), Hefei National Laboratory for Physical Sciences at the Microscale, and Synergetic Innovation Center of Quantum Information and Quantum Physics, University of Science and Technology of China, Hefei 230026, China*
[3]*Key Laboratory of Strongly Coupled Quantum Matter Physics of Chinese Academy of Sciences, School of Physical Sciences, University of Science and Technology of China, Hefei 230026, China*
[4]*Jiangsu Provincial Key Laboratory for Nanotechnology, Nanjing University, Nanjing 210093, China*

(Received 9 March 2023; accepted manuscript online 23 March 2023)

Excitons in solid state are bosons generated by electron-hole pairs as the Coulomb screening is sufficiently reduced. The exciton condensation can result in exotic physics such as super-fluidity and insulating state. In charge density wave (CDW) state, 1T-$TiSe_2$ is one of the candidates that may host the exciton condensation. However, to envision its excitonic effect is still challenging, particularly at the two-dimensional limit, which is applicable to future devices. Here, we realize the epitaxial 1T-$TiSe_2$ bilayer, the two-dimensional limit for its $2 \times 2 \times 2$ CDW order, to explore the exciton-associated effect. By means of high-resolution scanning tunneling spectroscopy and quasiparticle interference, we discover an unexpected state residing below the conduction band and right within the CDW gap region. As corroborated by our theoretical analysis, this mysterious phenomenon is in good agreement with the electron-exciton coupling. Our study provides a material platform to explore exciton-based electronics and opto-electronics.

DOI: 10.1088/0256-307X/40/5/057101

Excitonic bound states created in semiconducting two-dimensional (2D) materials recently find extensive applications in the fields such as optoelectronics and valleytronics.[1–9] In the case that the energy gain to form the exciton is larger than the energy gap separating the electrons and holes, the excitons condense into the excitonic insulating phase at low temperature.[1,2,9] The exciton condensation can also occur in semimetals when the conduction and valence bands are very close or slightly overlapped,[1,10] as exemplified by the 1T-phase $TiSe_2$. The bulk 1T-$TiSe_2$ hosts a $2 \times 2 \times 2$ charge density wave (CDW) order at low temperatures.[11] The exciton condensation was considered to play an important role in its CDW transition,[12,13] in spite of the debatable mechanism.[14–26] However, to directly detect the exciton is very difficult since it is charge neutral.[27] Considering that excitonic excitation interacts with electrons, here we alternatively explore the excitonic effect on the electron energy band in 1T-$TiSe_2$. By means of high-resolution scanning tunneling spectroscopy (STS) and quasiparticle interference (QPI), we investigate the 1T-$TiSe_2$ bilayer, the 2D limit of the $2 \times 2 \times 2$ CDW state, and discover an extra state residing below the conduction band and within the CDW gap region. Based on the many-body theoretical calculations, we elaborate that this unexpected extra state can be understood as the coupling of electrons to an excitonic mode. This study indicates that the exciton is a stable and coherent collective mode in 1T-$TiSe_2$, which is necessary for formation of an exciton condensate and in turn provides the basis for a well-defined coherence exciton excitation.

The crystal structure of the 1T-$TiSe_2$ bilayer is illustrated in Fig. 1(a). The 1T-$TiSe_2$ monolayer hosts a sandwich structure composed of three atomic layers of Se–Ti–Se. Each Ti atom is coordinated octahedrally by six adjacent Se atoms. The 1T-$TiSe_2$ bilayer is formed by two monolayers stacked via van der Waals interaction.

During the epitaxial growth of 1T-$TiSe_2$ monolayers, RHEED patterns were recorded to *in situ* monitor the growing morphology, as depicted in Fig. 1(b). The sharp streaks, as marked by blue and red triangles for the BLG/SiC(0001) substrate (BLG: bilayer graphene) and 1T-$TiSe_2$ layers, indicate a two-dimensional growth mode. Figure 1(c) shows a typical topographic image of $\sim$1.6 monolayer 1T-$TiSe_2$. This surface is composed of both monolayer and bilayer morphologies (more STM data for various coverages can be found in Fig. S1 of the Supplementary Information). Figure 1(d) represents the high

†These authors contributed equally to this work.
*Corresponding authors. Email: slyu@nju.edu.cn; jxli@nju.edu.cn; scli@nju.edu.cn
© 2023 Chinese Physical Society and IOP Publishing Ltd

resolution STM images taken on the 1T-$TiSe_2$ bilayer, verifying the clear 2×2 CDW state. Such CDW periodicity can also be confirmed in the fast Fourier transform (FFT) of the STM images (see Fig. S2). The 1×1 periodicity can be identified at higher bias voltages, as displayed in the insets in Fig. 1(d). The line-scan profile of Fig. 1(e) measured along the red arrowed line in Fig. 1(c) shows that the step height of the second layer is ~ 0.64 nm, close to the bulk value of $\sim$ 0.60 nm.[28] The stacking order between the first and second layers, as illustrated in Fig. 1(f), is consistent with that for the bulk material.

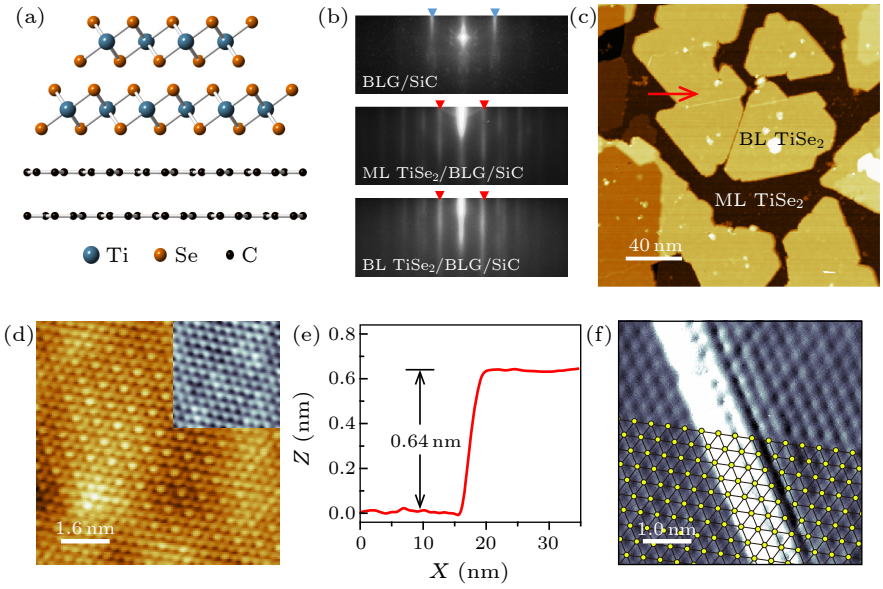

Fig. 1. STM topography of 1T-$TiSe_2$ bilayer epitaxially grown on the BLG/6H-SiC(0001) substrate. (a) Schematic illustration of the 1T-$TiSe_2$ bilayer on BLG/6H-SiC(0001). (b) RHEED patterns recorded on the bare BLG/6H-SiC(0001) substrate, the as-grown 1T-$TiSe_2$ monolayer (ML) and bilayer (BL), respectively. (c) Large-scale STM topographic image ($200 \times 200\,nm^2$, $U = +1$ V, $I_t = 100$ pA) taken on the surface of $\sim$1.6 MLs 1T-$TiSe_2$. (d) High-resolution STM image ($8 \times 8\,nm^2$, $U = +100$ mV, $I_t = 100$ pA) taken on the 1T-$TiSe_2$ bilayer, showing the 2×2 periodicity. Inset: atomic-resolution image ($3.5 \times 3.5\,nm^2$, $U = +200$ mV, $I_t = 100$ pA) showing the 1×1 periodicity. (e) Line-scan profile measured along the red arrowed line in (c) showing the step height of the second layer. (f) STM current image ($5 \times 5\,nm^2$, $U = +220$ mV, $I_t = 100$ pA) taken along the step edge between 1T-$TiSe_2$ bilayer and monolayer. The black mesh marks the lattice for the first and second layers and the yellow dots represent the atom positions, which shows that the stacking between the first and second layers is consistent with the bulk 1T structure.

To investigate the electronic structure of the 1T-$TiSe_2$ bilayer, STS and angle-resolved photoelectron spectroscopy (ARPES) measurement were carried out. The according data taken on the 1T-$TiSe_2$ monolayer can be found in Fig. S3 for comparison. Figure 2(a) shows the dI/dV differential spectrum taken on the 1T-$TiSe_2$ bilayer, representing the local density of state (DOS). The characteristics in the unoccupied state (positive bias) are the peaks at $\sim +0.62$ V and $\sim +1.58$ V originated from the Ti 3*d* orbitals. In the occupied state (negative bias), the dI/dV intensity sharply increases as the bias decreases to ~ -0.55 V, due to the more contribution from the Se 4*p* orbitals. These features are well comparable with the DFT calculated energy band of Fig. 2(b), through the integrated DOS of Fig. 2(c), see more DFT calculated results in Fig. S4. Our STS data for the monolayer and bilayer are both consistent with the previous study.[29] High-resolution dI/dV differential spectra near Fermi energy are depicted in Fig. 2(d), where two bump-like features are clearly identified at ~ -59 mV and ~ -225 mV (marked by red triangles). Moreover, a V-shaped suppression at Fermi energy is also observed, which is similar to the previous studies on the bulk 1T-$TiSe_2$.[25,30]

The ARPES result taken on the 1T-$TiSe_2$ bilayer, with a coverage of $\sim$2.0 ML, along the Γ–M direction in the 1×1 Brillouin zone, as shown in Fig. 2(e), shows the hole-like valence band at the Γ point and the electron-like conduction band at the M point. The band folding of the valence band at the M point verifies the 2×2 CDW state. The M point is renamed as the zone center of Γ^* in the new 2×2 Brillouin zone. The energy distribution curves (EDCs) at the Γ (blue dashed line) and M (orange dashed line) points are depicted in Fig. 2(d), where the conduction band minimum (CBM) and valence band maximum (VBM) are extracted at ~ -55 mV and ~ -230 mV, respectively. The CDW gap is thus determined to be $\sim$175 mV for the 1T-$TiSe_2$ bilayer. Compared the ARPES EDCs with STS spectrum in Fig. 2(d), it is turned out that the bump-like features in the STS data correspond exactly to the edges of the CDW gap. Similarly, the magnitude of the CDW gap in the 1T-$TiSe_2$ monolayer, determined in the same way, is $\sim$195 mV, con-

sistent with the previous report[31,32] as well, see Fig. S3 in the Supplementary Information for more detail.

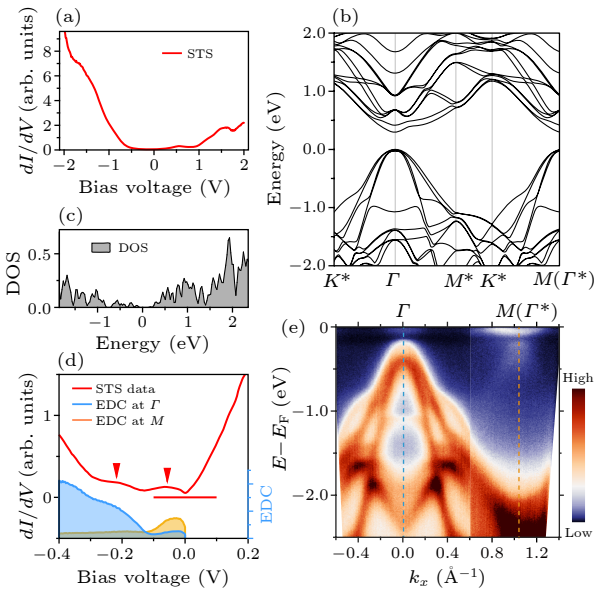

Fig. 2. Electronic structure of the epitaxial 1T-$TiSe_2$ bilayer on BLG/6H-SiC(0001). (a) Differential dI/dV spectrum taken on the 1T-$TiSe_2$ bilayer in large bias range ($U = +1$ V, $I_t = 200$ pA, $U_{mod} = 12$ mV). (b) DFT-calculated band structure for the 1T-$TiSe_2$ bilayer in CDW phase. (c) DFT calculated density of state based on the bands structure in (b). (d) Differential dI/dV spectrum ($U = +200$ mV, $I_t = 200$ pA, $U_{mod} = 7$ mV) near Fermi level obtained on the $TiSe_2$ bilayer (red), and the energy distribution curves (EDCs) extracted from the ARPES results (e) at high symmetric points of Γ and M, as marked by the dashed blue and orange lines in (e). (e) ARPES result taken on the $TiSe_2$ bilayer along the M–Γ–M direction at $\sim$ 8 K. The blue and orange dashed lines mark the positions where the EDCs in (d) are taken.

We further explore the detailed electronic structure near the CDW gap via the STS-QPI technique. The dI/dV maps at various energies were collected on the 1T-$TiSe_2$ bilayer (see Fig. S5). Figure 3(a) represents the FFT image of a typical dI/dV map (more FFT results can be found in Figs. S6 and S7). Besides the Bragg and CDW points, the FFT image exhibits the QPI signatures as well. The overall QPI pattern can be well reproduced by the simulation [Fig. 3(b)] based on the DFT calculated constant energy contours (Fig. 3(c) and Fig. S4). The three main features in Figs. 3(a) and 3(b), as marked by different colored arcs in Fig. 3(b), are contributed by different inter-pocket scattering of electrons in the conduction bands. The corresponding scattering processes are also illustrated by the same colored arrows in Fig. 3(c). The red rectangle in Fig. 3(a) highlights the characteristic petaloid feature, which is mainly associated with the electron scattering between the diagonal pockets of the conduction band in the Brillouin zone, as marked by q_1 in Fig. 3(c). Figure 3(e) shows the stacking of the FFT images in this select rectangle at various energies, where the petaloid feature, as marked in its bottom half by red arc, is adopted to make a quantitative analysis. The petaloid becomes smaller and moves towards the Bragg point as the bias voltage decreases, confirming its electron-like band origin. Figure 3(d) shows the corresponding DFT simulated patterns. It is found that the QPI results are consistent very well with the DFT simulations for the bias region above the CDW gap, in comparison of Fig. 3(d) (i–iv) and Fig. 3(e) (i–iv). Quantitative determination of the petaloid feature is plotted in Fig. 3(f). Parabolic fitting gives the minimum at ~ -60 mV, in good agreement with the conduction band minimum of ~ -55 mV as determined in ARPES and STS measurements.

Surprisingly, besides the energy band-associated QPI signatures, there appears another extra QPI feature residing below the conduction band, as marked by the orange arcs in Fig. 3(e) (v and vi). The extra feature is found to be overall similar to the aforementioned petaloid, but with a systematic lower energy. According to the STS and ARPES measurements, the extra state is found to locate right within the CDW gap, where no state should be expected under the single-electron frame, and therefore the DFT simulation cannot reproduce these patterns. However, due to the subtle difference of growth kinetics, the first layer $TiSe_2$ hosts much less natural defects as the interference centers, and thus no distinguishable QPI signals were obtained in $TiSe_2$ monolayer. We emphasize that the bilayer $TiSe_2$ is the true single unit of the bulk $2 \times 2 \times 2$ CDW state. Although the monolayer $TiSe_2$ exhibits a 2×2 CDW state as well, the bilayer $TiSe_2$ is the focus of our study.

Because the extra state is located right within the CDW gap, the possibility of coming from the split bands for the $TiSe_2$ bilayer at M point [Fig. 2(b)] can be easily excluded. Extrinsic effects that would be plausible to induce a non-zero intensity within the gap can be easily ruled out. The tip induced band bending effect, which may result in an apparently reduced gap, is found to be not prominent, according to the tip-height-dependent measurement in Fig. S8. The possible substrate's contribution to the tunneling spectroscopy can be easily ruled out because it would otherwise exponentially decay with the thickness of the epitaxial layer. In fact, the observed absence of a full gap in the second layer 1T-$TiSe_2$ looks very similar to the first layer. The band gap of $\sim$ 175 mV is incredibly larger than the thermal broadening at $\sim$4 K. The impact of impurities, as has been argued in the bulk $TiSe_2$,[30] was not considered, because our STS spectra were collected in the defect-free regions, see Fig. S9. Therefore, it is deduced that the extra QPI features, as well as the finite LDOS within the CDW gap, are resulted from the intrinsic electronic state of 1T-$TiSe_2$ bilayer. Unfortunately, it is challenging to distinguish such a state in ARPES spectra shown in Fig. 2(e), because the low intensity of the state and limited resolution of ARPES instrument will submerge the state under the broadening of CBM and VBM peaks and the background noise induced by surface defects and boundaries. Even so, it is noteworthy that adding a state within the CDW gap gives a better fitting to the EDC curves at Γ and M, thus suggesting the extra in-gap state. According to the EDC fitting, this extra state is more prominent at M than at Γ (details of fitting can be seen in Fig. S13).

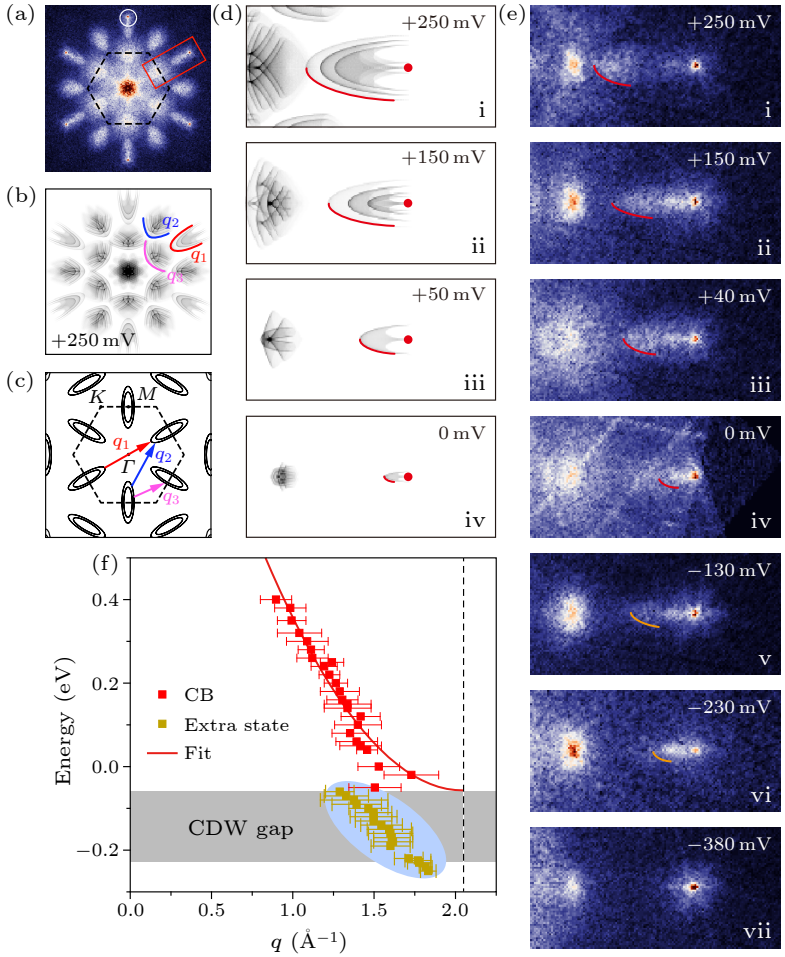

Fig. 3. STS-QPI pattern and DFT simulation of the 1T-$TiSe_2$ bilayer. (a) Drift corrected and symmetrized fast Fourier transform (FFT) images of the dI/dV maps taken at $U = +250$ mV. The Bragg points is marked by white circle. The red rectangle marks the characteristic QPI pattern along Γ–M. [(b), (c)] Simulated QPI result and the corresponding DFT calculated constant energy contour (CEC) for +250 mV. The q vectors indicate the scattering wave vectors, as marked by different colors. The black dashed hexagon represents the first Brillouin zone. [(d), (e)] A series of DFT-simulated and STS-experimental QPI patterns as marked in the red rectangle in (a) at various biases. The red dots mark the Bragg points. The red (orange) half arcs mark the QPI features originated from the interference of electrons in the conduction band (extra state). (f) E–q dispersion along Γ–M direction. The red (orange) dots represent the evolution for the conduction band (extra state). The red solid line is the parabolic fitting. The vertical black dashed line marks the position of the Bragg point.

It is well known that the coupling of electrons to a bosonic mode, such as phonons or excitons, can lead to the renormalization of the electronic energy band,[33–35] we therefore explore such a picture of electron-boson coupling based on a phenomenological model given by

$$H = \sum_{k\sigma} \varepsilon_k c^\dagger_{k\sigma} c_{k\sigma} + \sum_q \omega_q \left(b^\dagger_q b_q + \frac{1}{2} \right) + \sum_{kq\sigma} g_{k,q} c^\dagger_{k+q,\sigma} c_{k\sigma} (b_q + b^\dagger_{-q}), \quad (1)$$

where ε_k is the dispersion of the conduction or valence band, ω_q the dispersion of the bosons, and $g_{k,q}$ the electron-boson coupling constant. We only consider the nearest-neighbor hopping (t) and next-nearest-neighbor hopping (t') in the tight-binding model, and omit the momentum-dependence of ω_q and $g_{k,q}$, i.e., $\omega_q = \Omega_0$ and $g_{k,q} = g_0$. The calculated conduction-band spectra around M via the virtual exchange of a boson are shown in Fig. 4(a) and Fig. S11 (details of the calculation can be seen in Methods and Measurement of the Supplementary Information). When Ω_0 is low and $-\Omega_0$ is above the CBM, two kink features are formed in the conduction band at $\pm\Omega_0$, and meanwhile the energy band near the CBM bottom becomes blurred [see Fig. S11(a)]. As Ω_0 is increased to make $-\Omega_0$ below the CBM, an isolated extra state starts to emerge, forming a lower branch within the CDW gap, as shown in Fig. 4(a) and Fig. S11(b). Further increasing Ω_0 makes the lower branch move downward, with a prominently decreased spectral weight [see Fig. S11(c)]. In contrast, the calculated valence-band spectrum around Γ, as shown in Fig. 4(b), exhibits only a weak kink at the energy of Ω_0 below the VBM. This is different from the conduction band because the valence band is completely filled. The calculation result does not qualitatively change if considering the exciton band dispersion,[36] see Fig. S11.

The experimental result shown in Fig. 3(f) is qualita-

tively consistent with the theoretical spectrum shown in Fig. 4(a), where the lower branch behaves as the extra state. Moreover, the simulated QPI patterns generated from the lower branch (Fig. S12), also well reproduce the experimental QPI results for the in-gap extra state, which is however not accessible in the first-principle DFT calculation. Unlike the separate state within the CDW gap, the kink feature in the valence band, as illustrated in Fig. 4(b), is too slight to experimentally identify. The agreement between the many-body calculations and experimental results confirms that the in-gap extra state comes from the electron-boson coupling. It is noteworthy that the experimental in-gap extra state looks like dispersive, but the theoretical result does not. Since we adopted a simplified model without considering the momentum dependence of the electron-exciton coupling and the exciton dispersion, the obtained electron self-energy exhibits a rather weak dispersion, which deviates from the experimental results.

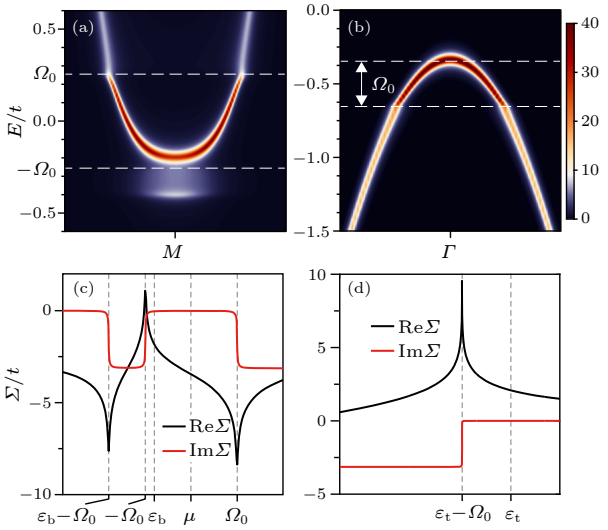

Fig. 4. Theoretical results based on the electron-boson coupling model. [(a), (b)] The renormalized electron spectra based on the electron-boson coupling model Eq. (1) for conduction and valence bands, respectively. [(c), (d)] The zero-temperature self-energies with a constant DOS for conduction and valence bands, respectively. Here $\Omega_0 = 025t$ and $g_0 = 0.5t$ are used. The colorbars in (a) and (b) present the spectral intensity, and the dimension of the spectral intensity is the reciprocal of energy. An arbitrary unit is used in the colorbars, in which the nearest-neighbor hopping of the conduction-band electrons is set to 1.

To further unveil how the bosonic mode energy impacts on the extra state formation, we adopted a constant DOS D to simplify the analytical formula of self-energy for electrons due to the coupling to the boson, as

$$\Sigma(k,\omega) = g_0^2 D \ln\left(\frac{\omega-\Omega_0+i0^+}{\omega+\Omega_0+i0^+}\cdot\frac{\omega+\Omega_0-\varepsilon_b+i0^+}{\omega-\Omega_0-\varepsilon_t+i0^+}\right) \quad (2)$$

for conduction band, and

$$\Sigma(k,\omega) = g_0^2 D \ln\left(\frac{\omega+\Omega_0-\varepsilon_b+i0^+}{\omega+\Omega_0-\varepsilon_t+i0^+}\right) \quad (3)$$

for valence band, where ε_t and ε_b are the top and bottom energies of the conduction band in Eq. (2) and valence band in Eq. (3). The results extracted from Eq. (2) are shown in Fig. 4(c). There exist four step discontinuities in the imaginary part (ImΣ) of the self-energy, and four corresponding extremes in the real part (ReΣ). The magnitude of the extreme at $-\Omega_0$ is so small that the spectrum in Fig. 4(a) shows no visible feature at this energy. Nevertheless, the effect of the extreme at $+\Omega_0$ is to renormalize the bare energy band (ε_k), following its dispersion $\omega = \varepsilon_k + \text{Re}\Sigma\,(k,\omega)$, and to result in a kink feature at $+\Omega_0$ in Fig. 4(a). Since the energy of $-\Omega_0+\varepsilon_b$ is below CBM, where there is no bare energy band, an extra state is generated, as shown in Fig. 4(a). The spectrum at $\Omega_0+\varepsilon_t$, is irrelevant, due to its higher energy. The results extracted from Eq. (3) are shown in Fig. 4(d). According to Eq. (3), ReΣ has two extremes at $\varepsilon_t+\Omega_0$ and $\varepsilon_b+\Omega_0$, so there is no extra state at Γ resulting from the valence band. The absence of an extra state in the CDW gap near Γ is in good agreement with the ARPES measurement.

In our theoretical calculation, we provided a qualitative analysis of the electron-exciton coupling. The exciton excitations are the collective propagators originating from the particle-hole excitations with one electron in the conduction band and one hole in the valence band, and the effective electron-exciton couplings for the conduction-band and valence-band electrons stem from the inter-band Coulomb interactions. It should be pointed out that the inter-band Green's function, which is nonzero in the excitonic insulators due to the exciton condensation, plays an essential role to produce the intra-band electron-exciton couplings from the inter-band Coulomb interactions. It is difficult to give a quantitative strength of the electron-exciton coupling, partially due to a lack of a theoretical and/or experimental evidence. Noticeably, it seems not likely that the coupling strength can be drastically lower, since the electron-exciton coupling can be derived formally from the electron–electron interactions, which also determines the charge gap between the conduction and valence bands. On the other hand, the conduction band comes from the 3d orbitals of Ti, for which the hopping integrals are much smaller than the electron–electron interactions. It thus also seems acceptable that the coupling strength g is on a similar order of magnitude as the hopping t. In fact, in wide range of g, for instance from $0.1t$ to $0.8t$, our calculation shows the qualitatively consistent spectral results with the main difference in the intensity of the additional in-gap spectra.

In general, either phonons or excitons can contribute a bosonic mode. The experimentally determined extra state bottom at ~ -230 mV and CBM at ~ -60 mV gives the energy of Ω_0 to be ~ 170 meV, much larger than the phonon energies of $<\sim 30$ meV as reported in 1T-$TiSe_2$.[15,20,23,35] The formation of an exciton, a bound state of an electron-hole excitation, is signified by the divergence of the renormalized electron-hole susceptibility.[34,37,38] Thus, the exciton mode should fall into the gap between the Fermi level and VBM. Considering our extracted upper limit of ~ 170 meV for Ω_0, the binding energy of exciton is estimated to be larger than $\sim$ 60 meV, in agreement with the previous calculation of ~ 75 meV for 1T-$TiSe_2$ monolayer.[39,40] Unfortunately, the binding energy of exciton in 1T-$TiSe_2$ bilayer has not been reported either ex-

perimentally or computationally. The Coulomb attraction between electrons and holes is usually decreased in bilayer compared to monolayer, due to an enhanced Coulomb screening. Thus a binding energy of exciton, slightly less than 75 meV, is expected in 1T-$TiSe_2$ bilayer. It is well-known that the extrinsic effects, such as substrates, can change the exciton binding energy.[41–44] Similarly, these extrinsic effects can change the band gap of 2D materials as well.[41–44] According to the band gap size of $\sim$175 meV as determined in our work, previous calculation predicts an exciton binding energy of $\sim$90 mV and $\sim$3 mV for the screening parameter of $\mu = 0$ and 0.2 $Å^{-1}$, respectively.[39] Our experimentally determined binding energy of $\sim$60 mV is located between the calculated values, thus suggesting that the exciton is not quenched in the epitaxial $TiSe_2$ bilayer by the substrate. According to the quantitative comparison of binding energy, the electron-exciton coupling is strongly suggested to be the origin of the observed extra state. Although there is no formal difference between the electron-exciton and electron-phonon couplings in our model Hamiltonian, they are in principle distinguishable in detail. For example, the excitons come from the particle-hole excitations between the conduction and valence bands, and therefore the doping of charge carriers can be applied to tune the exciton energy. In contrast, the phonon energy does not change with doping. The coupling of electrons with other bosons, such as phonon, is beyond the focus of our study. Nevertheless, it deserves a future extensive investigation in $TiSe_2$ or related materials.

The extra state we observed is in fact essentially different from the recently reported replica bands.[45,46] Their replica bands are in the nonequilibrium state of a band insulator, where the electrons are excited out of the valence bands to form the exciton states. Our work is focused on how the exciton excitations affect the spectral characteristics of the equilibrium-state electrons. The extra states we observed originate from the coupling between electrons and excitons, rather than a replica band of the valence band. These states already exist in the equilibrium state.

In summary, by means of high-resolution STS-QPI in combination with theoretical analysis based on many-body analysis, we have unveiled the exciton mode via its coupling to the electron band of 1T-$TiSe_2$ bilayer, which allows for a profound understanding in its electronic properties, and arouses a new thought about exploration of exciton-based electronic and optoelectronic applications.

Acknowledgements. We thank Zhengyu Weng for fruitful discussions. This work was supported by the National Key Research and Development Program of China (Grant Nos. 2021YFA1400403, 2018YFA0306800, 2019YFA0210004, and 2016YFA0300401), the National Natural Science Foundation of China (Grant Nos. 92165205, 11774149, 11790311, 11774154, 11674158, and 12074175), and Innovation Program for Quantum Science and Technology (Grant No. 2021ZD0302800)

References

[1] Kohn W 1967 *Phys. Rev. Lett.* **19** 439
[2] Eisenstein J P and MacDonald A H 2004 *Nature* **432** 691
[3] Butov L V 2004 *J. Phys.: Condens. Matter* **16** R1577
[4] Chen H L, Wen X W, Zhang J, Wu T M, Gong Y J, Zhang X, Yuan J T, Yi C Y, Lou J, Ajayan P M, Zhuang W, Zhang G Y, and Zheng J R 2016 *Nat. Commun.* **7** 12512
[5] Combescot M, Combescot R, and Dubin F 2017 *Rep. Prog. Phys.* **80** 066501
[6] Kunstmann J, Mooshammer F, Nagler P, Chaves A, Stein F, Paradiso N, Plechinger G, Strunk C, Schüller C, Seifert G, Reichman D R, and Korn T 2018 *Nat. Phys.* **14** 801
[7] Rivera P, Yu H, Seyler K L, Wilson N P, Yao W, and Xu X 2018 *Nat. Nanotechnol.* **13** 1004
[8] Wang G, Chernikov A, Glazov M M, Heinz T F, Marie X, Amand T, and Urbaszek B 2018 *Rev. Mod. Phys.* **90** 021001
[9] Wang Z F, Rhodes D A, Watanabe K, Taniguchi T, Hone J C, Shan J, and Mak K F 2019 *Nature* **574** 76
[10] Zenker B, Ihle D, Bronold F X, and Fehske H 2012 *Phys. Rev. B* **85** 121102R
[11] Di Salvo F J, Moncton D E, and Waszczak J V 1976 *Phys. Rev. B* **14** 4321
[12] Rohwer T, Hellmann S, Wiesenmayer M, Sohrt C, Stange A, Slomski B, Carr A, Liu Y, Avila L M, Kallane M, Mathias S, Kipp L, Rossnagel K, and Bauer M 2011 *Nature* **471** 490
[13] Hedayat H, Sayers C J, Bugini D, Dallera C, Wolverson D, Batten T, Karbassi S, Friedemann S, Cerullo G, van Wezel J, Clark S R, Carpene E, and Como E D 2019 *Phys. Rev. Res.* **1** 023029
[14] Zunger A and Freeman A J 1978 *Phys. Rev. B* **17** 1839
[15] Holt M, Zschack P, Hong H, Chou M Y, and Chiang T C 2001 *Phys. Rev. Lett.* **86** 3799
[16] Kidd T E, Miller T, Chou M Y, and Chiang T C 2002 *Phys. Rev. Lett.* **88** 226402
[17] Cercellier H, Monney C, Clerc F, Battaglia C, Despont L, Garnier M G, Beck H, Aebi P, Patthey L, Berger H, and Forro L 2007 *Phys. Rev. Lett.* **99** 146403
[18] Li G, Hu W Z, Qian D, Hsieh D, Hasan M Z, Morosan E, Cava R J, and Wang N L 2007 *Phys. Rev. Lett.* **99** 027404
[19] Ishioka J, Liu Y H, Shimatake K, Kurosawa T, Ichimura K, Toda Y, Oda M, and Tanda S 2010 *Phys. Rev. Lett.* **105** 176401
[20] Weber F, Rosenkranz S, Castellan J P, Osborn R, Karapetrov G, Hott R, Heid R, Bohnen K P, and Alatas A 2011 *Phys. Rev. Lett.* **107** 266401
[21] Sugawara K, Nakata Y, Shimizu R, Han P, Hitosugi T, Sato T, and Takahashi T 2016 *ACS Nano* **10** 1341
[22] Fu Z G, Hu Z Y, Yang Y, Lu Y, Zheng F W, and Zhang P 2016 *RSC Adv.* **6** 76972
[23] Hellgren M, Baima J, Bianco R, Calandra M, Mauri F, and Wirtz L 2017 *Phys. Rev. Lett.* **119** 176401
[24] Kolekar S, Bonilla M, Ma Y J, Diaz H C, and Batzill M 2018 *2D Mater.* **5** 015006
[25] Zhang K W, Yang C L, Lei B, Lu P C, Li X B, Jia Z Y, Song Y H, Sun J, Chen X H, Li J X, and Li S C 2018 *Sci. Bull.* **63** 426
[26] Lian C, Zhang S J, Hu S Q, Guan M X, and Meng S 2020 *Nat. Commun.* **11** 43
[27] Kogar A, Rak M S, Vig S, Husain A A, Flicker F, Joe Y I, Venema L, MacDougall G J, Chiang T C, Fradkin E, van Wezel J, and Abbamonte P 2017 *Science* **358** 1314
[28] Stirling W G, Dorner B, Cheeke J D N, and Revelli J 1976 *Solid State Commun.* **18** 931
[29] Peng J P, Guan J Q, Zhang H M, Song C L, Wang L L, He K, Xue Q K, and Ma X C 2015 *Phys. Rev. B* **91** 121113
[30] Yan S, Iaia D, Morosan E, Fradkin E, Abbamonte P, and Madhavan V 2017 *Phys. Rev. Lett.* **118** 106405
[31] Chen P, Chan Y H, Fang X Y, Zhang Y, Chou M Y, Mo S K, Hussain Z, Fedorov A V, and Chiang T C 2015 *Nat. Commun.* **6** 8943
[32] Chen P, Chan Y H, Won M H, Fang X Y, Chou M Y, Mo S K, Hussain Z, Fedorov A V, and Chiang T C 2016 *Nano Lett.* **16** 6331

[33] Cuk T, Lu D H, Zhou X J, Shen Z X, Devereaux T P, and Nagaosa N 2005 *Phys. Status Solidi B* **242** 11
[34] Monney G, Monney C, Hildebrand B, Aebi P, and Beck H 2015 *Phys. Rev. Lett.* **114** 086402
[35] Zhao J, Lee K, Li J, Lioi D B, Karapetrov G, Trivedi N, and Chatterjee U 2019 *Phys. Rev. B* **100** 045106
[36] Hong J, Senga R, Pichler T, and Suenaga K 2020 *Phys. Rev. Lett.* **124** 087401
[37] Li J X and Gong C D 2002 *Phys. Rev. B* **66** 014506
[38] Zenker B, Ihle D, Bronold F X, and Fehske H 2011 *Phys. Rev. B* **83** 235123
[39] Pasquier D and Yazyev O V 2018 *Phys. Rev. B* **98** 235106
[40] Lian C, Ali Z A, and Wong B M 2019 *Phys. Rev. B* **100** 205423
[41] Park S, Mutz N, Schultz T, Blumstengel S, Han A, Aljarb A, Li L J, List-Kratochvil E J W, Amsalem P, and Koch N 2018 *2D Mater.* **5** 025003
[42] Qiu D Y, Jornada F H D, and Louie S G 2017 *Nano Lett.* **17** 4706
[43] Druppel M, Deilmann T, Kruger P, and Rohlfing M 2017 *Nat Commun.* **8** 2117
[44] Raja A, Chaves A, Yu J, Arefe G, Hill H M, Rigosi A F, Berkelbach T C, Nagler P, Schuller C, Korn T, Nuckolls C, Hone J, Brus L E, Heinz T F, Reichman D R, and Chernikov A 2017 *Nat. Commun.* **8** 15251
[45] Man M K L, Madeo J, Sahoo C, Xie K, Campbell M, Pareek V, Karmakar A, Wong E L, Al-Mahboob A, Chan N S, Bacon D R, Zhu X, Abdelrasoul M M M, Li X, Heinz T F, Jornada F H D, Cao T, and Dani K M 2021 *Sci. Adv.* **7** eabg0192
[46] Perfetto E, Sangalli D, Marini A, and Stefanucci G 2019 *Phys. Rev. Mater.* **3** 124601